


Waveguide modes spatially resolved by low-loss STEM-EELSDavid Kordahl ^{*}*Department of Physics and Engineering, Centenary College of Louisiana, Shreveport, Louisiana 71104, USA
and Department of Physics, Arizona State University, Tempe, Arizona 85287, USA*Duncan T. L. Alexander [†]*Electron Spectrometry and Microscopy Laboratory, Institute of Physics, Ecole Polytechnique Fédérale de Lausanne,
1015 Lausanne, Switzerland*Christian Dwyer [‡]*Electron Imaging and Spectroscopy Tools, PO Box 506, Sans Souci LPO, Sans Souci, NSW 2219, Australia*

(Received 5 November 2020; revised 25 March 2021; accepted 29 March 2021; published 12 April 2021)

In an era of new developments in nanomaterials analysis enabled by the unprecedented spatial and energy resolutions of electron energy-loss spectroscopy in the scanning transmission electron microscope (STEM-EELS), it remains that the vast majority of works concern collective or single-particle excitations that are well described by the electrostatic approximation, which neglects retardation and magnetic field effects. Here we demonstrate a simple case in which that approximation is fundamentally inadequate. When the beam energy is above the Cherenkov threshold and the geometric dimensions of the nanomaterial sample are on the order of the wavelength of light in the material, spatial variations in low-loss ($\lesssim 5$ eV) spectral maps from guided light modes may be observed. We demonstrate such observations for amorphous silicon disks and offer an interpretation of the results based on the waveguide modes of a cylinder. We also demonstrate explicitly that spatial variations from waveguide modes are manifest in analytic models for the especially simple geometry of a STEM beam penetrating a dielectric ribbon. We discuss how these modes relate to those that have been observed more generally in dielectric nanomaterials.

DOI: [10.1103/PhysRevB.103.134109](https://doi.org/10.1103/PhysRevB.103.134109)**I. INTRODUCTION**

In recent decades, innovations in electron energy-loss spectroscopy in the scanning transmission electron microscope (STEM-EELS) have enabled significant advances in existing spectroscopic techniques to probe nanomaterials and have also opened doors to new ones. Correction of the spherical aberration intrinsic to round electron lenses [1,2] has enabled subatomic-sized electron beams facilitating atomic-resolution core-level mapping [3–8], and the introduction of monochromators [9,10] has led to deep sub-100 meV (and even near-meV) energy resolution—and the new field of vibrational spectroscopy in the electron microscope [11,12]. Together, high spatial and energy resolutions have allowed the plasmonic [13–17] and vibrational [18–27] modes of various nanoscale materials to be mapped in detail. Used alongside techniques like cathodoluminescence, such techniques now allow investigators to converge on robust descriptions of nanoscale materials systems [28,29].

Alongside these experimental innovations, continued advances in theory and computational methods have allowed

theory and experiment to be closely compared. For plasmon mapping using low-loss STEM-EELS, which is of particular relevance here, both the discrete dipole approximation [30,31] and the boundary element method [32,33] have been implemented, allowing electrodynamic effects to be captured in numerical simulations. For a precise match between theory and experiment, an electrodynamic approach is undoubtedly required. Yet in reviews of the literature [17,34], it is striking how successful the electrostatic approximation (i.e., the approximation where the speed of light $c \rightarrow \infty$) has been in describing the essential physics for many nanomaterials geometries, despite its neglect of retardation and magnetic fields. Indeed, apart from nanomaterials geometries that are specifically tailored to generate electrodynamic effects (e.g., photonic crystals [35] or metallic arrays [36]), theoretical treatments that compare the electrostatic and electrodynamic approaches [22,37,38] have reported only modest differences in the predicted STEM-EELS signals, with the incorporation of electrodynamic effects often just redshifting modal frequencies and lowering spectral intensities of the electrostatic prediction by a few percent.

By contrast, silicon nanocavities are known to have Mie-like resonances that can be excited by electrons [39], and new STEM-EELS measurements by Flauraud and Alexander [40,41] on amorphous silicon disks show electrodynamic effects that cannot be captured by the electrostatic

^{*}dkordahl@centenary.edu[†]duncan.alexander@epfl.ch[‡]dwyer@eistools.com

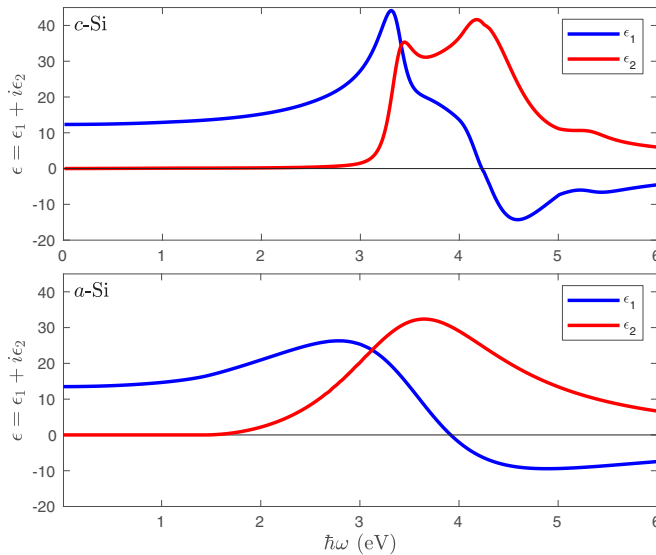


FIG. 1. Dielectric functions of crystalline silicon [44–46] (top) and amorphous silicon (bottom). Real parts of the measured values are plotted in blue, and imaginary parts are plotted in red.

approximation. In the constituent datasets of the latter work, spectral maps in the low-loss region <2.4 eV were obtained from amorphous silicon disks with diameters in the range 100–500 nm. These maps superficially resemble those predicted from the surface modes of thin disks [42] or oblate spheroids [43]. Crucially, however, surface modes in the electrostatic approximation require the real part of the dielectric function to be negative at the resonance frequency, whereas silicon has a dielectric function that is positive and increasing in the energy range of interest, as shown in Fig. 1. Hence, the results of Flauraud and Alexander are not attributable to electrostatic surface modes. Further explanation is needed.

The purpose of this paper is twofold: first to explore models of waveguide modes in STEM-EELS theoretically, in both continuum semiclassical and discretized normal-mode approaches, and second to explore how such models compare to the experimental observations of silicon disks, whose measurements are further explored here. In Sec. II we briefly review how the waveguide modes manifest in well-known analytic solutions for a relativistic electron beam penetrating a dielectric ribbon. Although a Si layer surrounded by SiO_2 has been treated electrostatically in previous works [47,48], the ability of classical Fermi-type loss models to capture the spatial features of waveguide modes seems to have gone previously unremarked. In Sec. III, we develop a waveguide-mode model for an electron beam running parallel to the wall of a circular cylinder, and in Sec. IV we compare the results of this model with the previously reported measurements on silicon disks. We find good qualitative agreement between the trends in data for modes imaged across five separate disks, although, as we discuss in Sec. V, further numerical work is needed to address the details of how the relative energies of modes shift with changes in particle aspect ratios.

We show here how waveguide models can guide our thinking about where electrodynamic effects will be most significant in STEM-EELS, granted a few pertinent concessions.

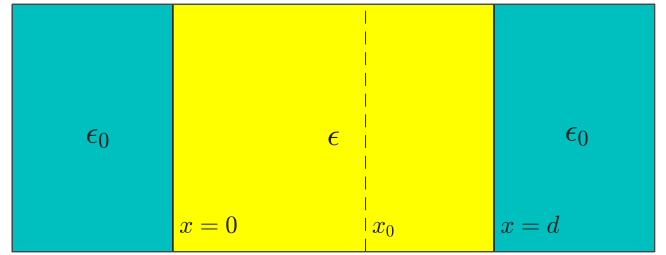


FIG. 2. Ribbon geometry, with ribbon material characterized by the dielectric function ϵ from $x = 0$ to $x = d$, surrounded by a material with the dielectric function ϵ_0 . The geometry is pictured here in cross section. The electron beam runs parallel to the z axis, piercing the ribbon at $x = x_0$, and is illustrated as a dashed vertical line.

Experimentally observed samples necessarily have a finite thickness, whereas the waveguide models assume an infinite thickness. Hence it is understandable that these models will not capture the experimentally observed mode frequencies precisely. Additionally, since waveguide models are quasianalytic, they are ill suited to the treatment of more complex sample geometries, as also explored with new STEM-EELS measurements [41]. Nonetheless, our approach already captures most of the trends in the low-order modes of simple geometries and leads us to a generic observation: When the STEM beam energy exceeds the Cherenkov threshold for a given material ($v > c/\sqrt{\epsilon}$) and the dimensions of the material are close to the wavelength of light in the material ($d > \pi c/\omega\sqrt{\epsilon}$), we should expect to observe guided light modes in low-loss STEM-EELS. In this regime, electrostatic interpretations will prove fundamentally inadequate.

II. DIELECTRIC RIBBON

The problem of a classical electron beam running parallel to a dielectric surface has been treated in both electrostatic [49] and electrodynamic [50] approaches and has been extended to account for arbitrarily many parallel layers [51]. Our interest in this geometry is as a simple test case to explore where electrodynamic effects become important, as revealed by comparing an electrostatic model to an electrodynamic one. For an electron traveling parallel to the z axis, this type of model solves for $d^2P/dz d\omega$, the electron energy loss per unit distance. When the integration limits over the ribbon thickness z grow large, the associated probabilities from $dP/d\omega$ can exceed unity. This can be interpreted as the number of expected scattering events for modes at the given energy [52].

Fermi-type loss models treat the electron classically and take the position of the beam relative to the interfaces (Fig. 2) and the dielectric functions as their input. The electron beam is treated as a point particle whose trajectory along $z = vt$ induces an electric field in the dielectric material it passes, consistent with standard boundary conditions. This excites a field that pushes back on the beam, causing energy loss. The loss spectrum is then extracted from the integrand of the work as

$$\frac{dP}{d\omega} = \frac{e}{\pi\hbar\omega} \text{Re} \left[\int_{-\infty}^{\infty} dz \exp(-i\omega z/v) E_z^{\text{ind}}(\mathbf{x}_0, z, \omega) \right]. \quad (1)$$

Enforcing electromagnetic boundary conditions allows surface effects to be conveniently captured by such models, although they implicitly include bulk effects as well.

In both the electrostatic and electrodynamic calculations (i.e., in calculations that both ignore and include retardation), the momentum transfer along the direction of electron flight is constrained to $k_z = \omega/v$. Integrating the expression for $d^2P/dz d\omega$ over a thickness L still leaves us with a sum over modes of varying transverse wave numbers k_y :

$$\frac{dP}{d\omega} = \frac{e^2 L}{\pi \hbar v^2} \text{Im} \left[\int_0^{k_y^{\text{cut}}} dk_y \chi_{\text{ribbon}}(k_y, x_0, \omega) \right]. \quad (2)$$

The cutoff k_y^{cut} is chosen to match the aperture size or to reflect the material's atomic scale, whichever is smaller. In the numerical examples below we have assumed a 150 μrad aperture, which determines the k_y cutoff as $k_y^{\text{cut}} = \theta_{\text{cut}} p/\hbar$, where p is the relativistic momentum of the electron.

When retardation is ignored, the calculation can be done using the electrostatic potential alone [49]. For a beam at x_0 with $0 \leq x_0 \leq d$ as in Fig. 2, the electrostatic Fermi model yields

$$\chi_{\text{ribbon}}^{\text{NR}} = \chi_{\text{bulk}} + \chi_{\text{surf}}, \quad (3)$$

where

$$\chi_{\text{bulk}} = \frac{1}{k} \left(\frac{1}{\varepsilon} \right),$$

$$\chi_{\text{surf}} = \frac{(\varepsilon^2 - \varepsilon_0^2)(e^{2kx_0} + e^{2k|(d-x_0)}) + 2(\varepsilon - \varepsilon_0)^2}{k\varepsilon[(\varepsilon - \varepsilon_0)^2 - (\varepsilon + \varepsilon_0)^2 e^{2kd}]}, \quad (4)$$

and where $k = \sqrt{k_y^2 + (\omega/v)^2} = |\mathbf{k}_{\parallel}|$, for a $\mathbf{k}_{\parallel} = (0, k_y, \omega/v)$.

When retardation is included, the theory of multilayered slabs from Bolton and Chen [51] can be simplified [48] to treat the same ribbon geometry pictured in Fig. 2 with

$$\chi_{\text{ribbon}}^{\text{R}} = \frac{1}{q\varepsilon k^2} \left\{ \varepsilon k_y^2 \left(\frac{v}{c} \right)^2 \frac{\tilde{\gamma}^- \tilde{\zeta}^+}{\tilde{L}^+ \tilde{L}^-} - q^2 \frac{\gamma^+ \zeta^-}{L^+ L^-} \right\} \quad (5)$$

in which

$$q = \sqrt{\mathbf{k}_{\parallel}^2 - \varepsilon(\omega/c)^2}, \quad q_0 = \sqrt{\mathbf{k}_{\parallel}^2 - \varepsilon_0(\omega/c)^2},$$

$$h^\sigma = q\varepsilon_0 + \sigma q_0\varepsilon, \quad \tilde{h}^\sigma = q + \sigma q_0, \quad (6)$$

where σ determines the signs used in these expressions (i.e., σ can be “+” or “-”), and

$$\gamma^\sigma = h^+ \exp(q(2d - x_0)) - \sigma h^- \exp(qx_0),$$

$$\zeta^\sigma = h^+ \exp(qx_0) + \sigma h^- \exp(-qx_0),$$

$$L^\sigma = h^+ \exp(qd) + \sigma h^-, \quad (7)$$

where the terms in Eq. (5) with tildes on top have the same form as their counterpart expressions in Eq. (7), except with h^σ terms replaced by \tilde{h}^σ as defined in Eq. (6).

In the limit where $c \rightarrow \infty$, the electrodynamic expression of Eq. (5) reduces to the electrostatic expression of Eq. (3). Bolton and Chen remark that the term with tildes is associated with the transverse electric (TE) waveguide modes, which travel in some direction $\hat{\mathbf{k}}_{\parallel}$ with $\mathbf{E} \cdot \hat{\mathbf{k}}_{\parallel} = 0$ and $E_x = 0$, and the term without tildes is associated with transverse magnetic (TM) modes, which travel in some direction $\hat{\mathbf{k}}_{\parallel}$ with

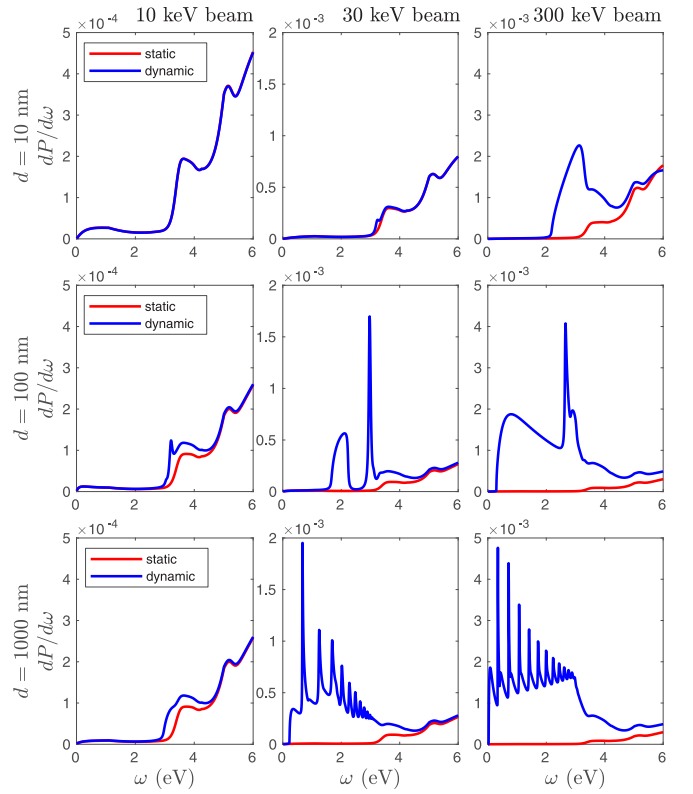


FIG. 3. Simulated spectra in electrostatic and electrodynamic approaches (plotted in red and blue, respectively), for beams of varying energy (left to right: 10 keV, 30 keV, 300 keV), penetrating the centers of c -Si ribbons of varying widths (top to bottom: 10 nm, 100 nm, 1000 nm) that are 100 nm thick. Spectra have units of inverse eV.

$E_z/E_y = k_z/k_y$ and $H_x = 0$. As with the electrostatic model, the electrodynamic model includes both “bulk” and “surface” effects, although this distinction is blurred for waveguide modes. In the bulk limit for a material with a real-valued dielectric function, the model of Bolton and Chen recovers the Frank-Tamm formula for Cherenkov losses of a relativistic electron [53].

Our numerical examples simulate electron energy-loss (EEL) spectra for an electron beam piercing a crystalline silicon ribbon surrounded by vacuum. For the c -Si dielectric function, we have used ellipsometry data [44,45] supplemented by model values [46] at low energies (Fig. 1). Results have been expressed as spectra by multiplying by a sample thickness of 100 nm, for electron beam energies of 10, 30, or 300 keV.

As can be seen in Fig. 3, electrodynamic corrections increase in importance as the beam energy increases and as the ribbon width increases. In the higher energy range where $\text{Re}[\varepsilon] < 0$, the electrostatic and electrodynamic models match qualitatively, hence the results are mainly captured by the bulk electrostatic contribution. We conclude that electrodynamic corrections are most significant in the range where $\text{Re}[\varepsilon] > 0$.

Where the electrostatic and electrodynamic predictions differ dramatically, the sharp spikes in the electrodynamic prediction arise from the TE modes, with a broad background from the TM modes. Predicted STEM-EELS maps across

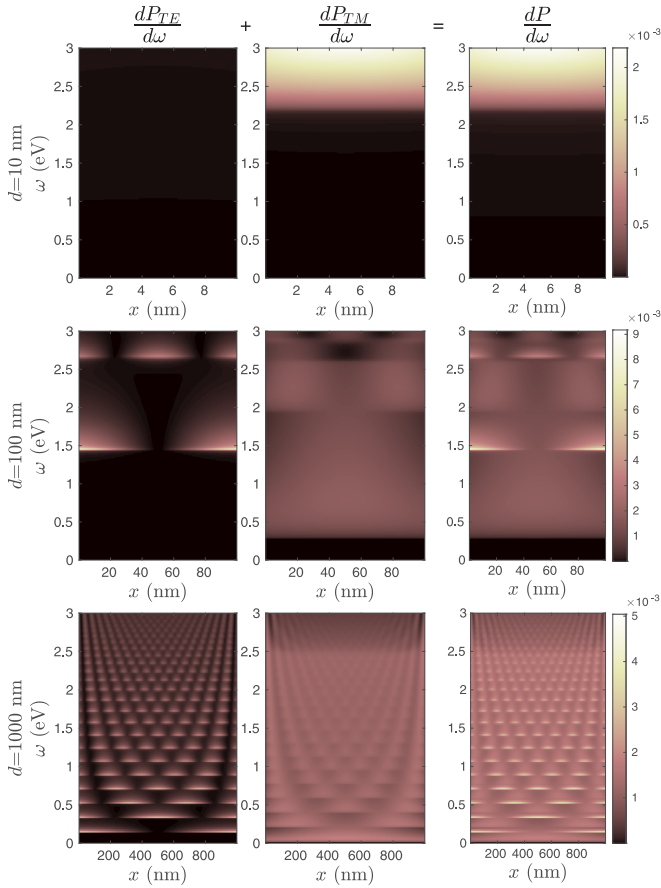


FIG. 4. Simulated spectral maps across 100 nm thick *c*-Si ribbons, for ribbons of varying widths (from top to bottom, $d = 10$ nm, 100 nm, 1000 nm), shown as the sum of contributions (right) from the TE waveguide modes (left) and TM waveguide modes (center). Spectra all assume a 300 keV beam and have units of inverse eV.

ribbons of differing widths for a 300 keV beam in Fig. 4 clearly show standing-wave patterns, with the onset of corresponding nodal patterns occurring at slightly lower energies for the TE modes and at slightly higher energies for the TM modes. But at low energies, an extra band of TM contributions without any nodes in E_z presents itself, which means that for thin layers the signal is dominated by TM mode contributions [48].

These plots feature intriguing shifts in modal frequencies. For one thing, the frequencies of observed modes decrease when the ribbon's width increases. This might be expected from the intuitive notion that longer wavelengths correspond to lower frequencies. We also notice that the frequencies of corresponding modes decrease when the beam energy increases. This may be less intuitively obvious, but in the excitation of waveguide modes discussed below, one can see more clearly how this results from physical constraints on momentum transfer along the direction of electron flight.

III. DIELECTRIC CYLINDER

In this section, we develop a simplified treatment of inelastic scattering from waveguide modes in a nonmagnetic dielectric cylinder of radius a surrounded by vacuum. In

Sec. IV we compare it with the data from amorphous silicon disks. While a full treatment would include contributions of the “leaky” modes [54] (or, with less interpretation, of the radiation modes), the mathematical details for these are unclear for modes lacking azimuthal symmetry [55]. Here we approximate the dielectric function for amorphous silicon by only using its real part, as extracted from ellipsometry data (see Fig. 1). This allows us to find the waveguide modes, which are the only contributions we have considered.

To derive the waveguide modes of a cylindrical dielectric rod, one can privilege the z components of the electric and magnetic fields, those components pointing along the cylindrical axis. To discretize these modes, one can introduce a fictitious length L_z over which all components are periodic, such that $k_z = 2\pi\ell/L_z$, where ℓ is some integer. All modes are also described via an azimuthal mode label m . Together, these lead to a spatial factor of $\exp(i(m\theta + k_z z))$ and a time dependence $\exp(-i\omega t)$. The radial dependence of field components is captured by the oscillatory function Bessel $J_m(k_r^< r)$ inside the cylinder and the decaying Bessel function $K_m(k_r^> r)$ outside the cylinder, where

$$k_r = \begin{cases} k_r^< = \sqrt{\varepsilon(\omega)\omega^2/c^2 - k_z^2}, & r \leq a \\ k_r^> = \sqrt{k_z^2 - \omega^2/c^2}, & r > a \end{cases} \quad (8)$$

and where ω is the eigenfrequency for a mode.

Once the z components of the modes have been fixed, the other components follow [56,57], and self-consistent boundary conditions determine the mode frequencies. For the $m = 0$ modes (i.e., the modes with azimuthal symmetry), the modes are either transverse electric (TE) or transverse magnetic (TM). The TE modes are defined by the fact that $E_z = 0$; they cannot be excited by an electron beam running parallel to the cylindrical axis. But the TM modes have an oscillatory E_z and $H_z = 0$, and can be imaged by a beam parallel to the cylindrical axis. The self-consistency condition for TM modes is

$$\left(\frac{\varepsilon J_0'(k_r^< a)}{k_r^< J_0(k_r^< a)} + \frac{1}{k_r^>} \frac{K_0'(k_r^> a)}{K_0(k_r^> a)} \right) = 0, \quad (9)$$

where the primes denote derivatives of the Bessel functions with respect to their arguments. This expression can be used to solve for mode frequencies. Notice that the condition that k_r is real-valued both inside and outside the cylinder sets the upper and lower limits on the mode frequencies as

$$\frac{k_z^2}{\varepsilon} < \frac{\omega^2}{c^2} < k_z^2, \quad (10)$$

which also applies for the hybridized modes discussed below.

Other modes, modes with azimuthal variation, cannot be categorized according to the TE/TM distinction. The general

eigenmode equation

$$\begin{aligned} & \left(\frac{1}{k_r^<} \frac{J'_m(k_r^< a)}{J_m(k_r^< a)} + \frac{1}{k_r^>} \frac{K'_m(k_r^> a)}{K_m(k_r^> a)} \right) \\ & \times \left(\frac{\varepsilon}{k_r^<} \frac{J'_m(k_r^< a)}{J_m(k_r^< a)} + \frac{1}{k_r^>} \frac{K'_m(k_r^> a)}{K_m(k_r^> a)} \right) \\ & = \frac{m^2 k_z^2 c^2}{a^2 \omega^2} \left(\frac{1}{(k_r^<)^2} + \frac{1}{(k_r^>)^2} \right)^2 \end{aligned} \quad (11)$$

can be solved to find allowed mode frequencies. Following Snitzer [57], the modes can be parameterized using a factor

$$P = \frac{\omega}{k_z c} \frac{|H_z|}{|E_z|} \quad (12)$$

that depends on the ratio of the z components of the magnetic and electric field amplitudes at the cylindrical surface ($|E_z|$ and $|H_z|$, respectively). We should expect P to diverge for the TE modes and to approach zero for the TM modes. For these hybridized modes, we label those modes that are more like the TE modes as the EH modes, defined by the fact that $1 < |P|$, and we label those modes that are more like the TM modes as the HE modes, defined by the fact that $0 < |P| < 1$.

Waveguide modes are typically labeled with two “quantum numbers”—e.g., TM_{mn} or HE_{mn} —that refer, respectively, to the azimuthal dependence (i.e., the factor of $\exp(im\theta)$) and the order of the solution (i.e., $n = 1$ labels the lowest-frequency solution for a given m and k_z , $n = 2$ labels the second-lowest-frequency solution, etc.) [58]. Solutions of different k_z but the same m and n often have the same qualitative features.

If we wish to simulate the STEM-EELS imaging of these modes, they must be correctly normalized [59]. In the projection approximation for a point probe at $\mathbf{x} = (x_0, y_0)$, the EEL transition probability in terms of these normalized electric field modes for mode labels ℓ (for k_z), m (for θ) and n (for solution number) leads to a transition probability [60] of

$$P_{\ell mn}(\mathbf{x}) = \left(\frac{e}{\hbar \omega_{\ell mn}} \right)^2 \left| \int dz \exp(i\omega_{\ell mn} z/v) E_{\ell mn}^z(\mathbf{x}, z) \right|^2, \quad (13)$$

where, as above, v is the speed of the beam electron. From this, the STEM-EEL spectrum becomes

$$\frac{dP}{d\omega} = \sum_{\ell mn} P_{\ell mn}(\mathbf{x}) \delta(\omega - \omega_{\ell mn}). \quad (14)$$

The normalization introduces a factor of L_z in $P_{\ell mn}$, which leads to an expression of loss per unit length, $d^2P/dz d\omega$, and the integral over z picks out modes for which $k_z = \omega_{\ell mn}/v$.

Fig. 5 shows the essential features of this model. Using a simplified dielectric model where $\varepsilon = 11.7$ (this is ε_0 for a -Si), the dispersion relations for the azimuthal mode labels $m = 0$ and $m = \pm 1$ are plotted. The dashed black lines indicate the frequency limits at each value of k_z , as given by Eq. (10). The dashed dispersion curves in these plots represent the TE modes (blue, $m = 0$) and the EH modes (purple, $|m| \geq 1$), which are either not imaged (the TE modes) or imaged with low intensity (the EH modes). The solid dispersion curves in these plots represent the TM modes (red, $m = 0$) and the

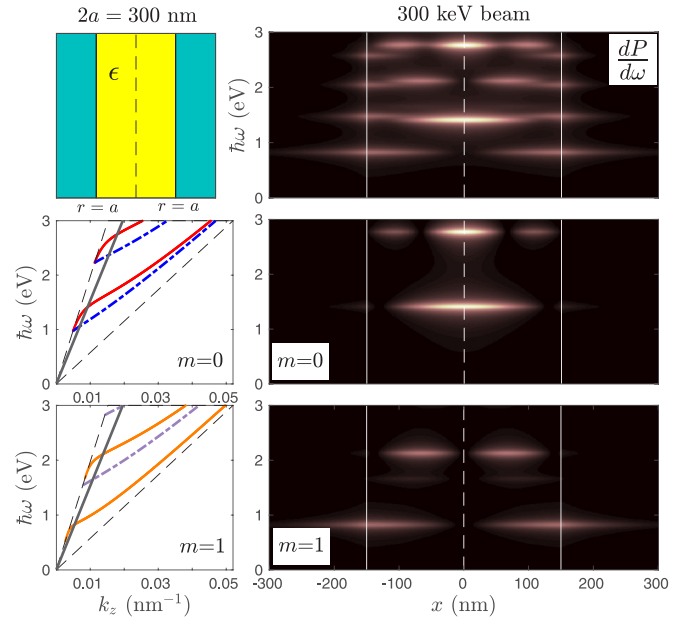


FIG. 5. Theoretical dispersion relations and line-scan spectra for an unbounded cylinder (see cartoon, top left). The cylinder has a diameter $2a = 300$ nm and an unvarying dielectric constant $\varepsilon = 11.7$. For the azimuthal mode labels $m = 0$ and $m = \pm 1$, dispersion relations are displayed in the leftmost column, with the $m = 0$ TE modes plotted as dashed blue lines and TM modes plotted as solid red lines, and with the EH and HE modes of the $m = \pm 1$ dispersion relations plotted as purple dashed lines and solid orange lines, respectively. A gray line intersects these curves to pick out the modes that are imaged for a 300 keV beam. The spectral contributions from modes with $m = 0$ and $m = \pm 1$ are shown on the same rows as their dispersion relations, and the summed contributions (along with higher-order m modes) are shown on the top row, where it can be seen that the TM_{0n} and HE_{1n} contributions dominate.

HE modes (orange, $|m| \geq 1$), which together dominate the spectra.

The bottom two rows of the theoretical line-scan spectra on the right of Fig. 5 show the contributions from $m = 0$ and $m = \pm 1$ modes, as imaged by 300 keV beams. The modal contributions have been broadened by 0.1 eV. These beam energies are reflected in the dispersion relation plots as gray lines. The gray lines intersect dispersion curves where the $k_z = \omega_{\ell mn}/v$ condition is fulfilled. These plots show why modes appear at lower energies for a higher energy beam, since a higher beam energy increases the slope of the intersecting gray line. Notice that the summed contributions from $m = \pm 1$ modes lead to azimuthal symmetry in the measurements even though the modes themselves vary azimuthally.

IV. DISK MEASUREMENTS

A 300 keV convergent STEM probe ($\alpha \approx 17$ mrad) was deployed on five silicon disks whose diameters ranged from 100–500 nm. EEL spectra were recorded using a collection angle of ~ 22 mrad. (Further specifications are provided in our references [40,41].) Energies of the lowest-order modes are sufficiently separated in the EEL spectra that we can track them across disks of various sizes. Since experimental disk

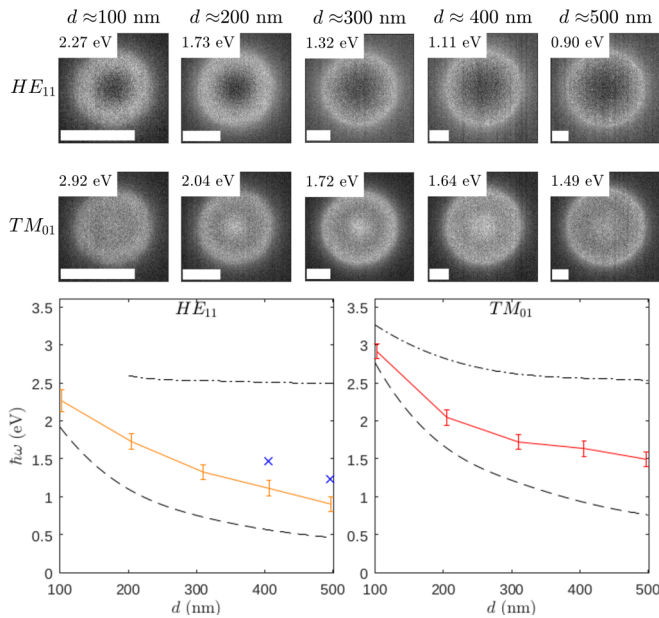


FIG. 6. For five disk diameters (scale bars represent 100 nm), we show the HE_{11} -type mode maps (top row) and the TM_{01} -type mode maps (second row) as found directly in the STEM-EELS data, summed over an energy window shown by the error bars on the data points in the bottom row. In the bottom row, the experimental frequencies are shown between theoretical predictions for the infinite rod (lower dashed curve) and the thin disk (upper dot-dashed curve). On the HE_{11} plot, two blue \times 's represent additional modes resembling those of the top row, which are visible only in the wider disks.

thicknesses must be finite, energies predicted for a mode type in the waveguide model with $k_z = \omega_{\ell mn}/v$ should be seen as lower bounds on the modes for the measured disks. For an upper bound on mode energies in the measured disks, we used the “thin disk” approximation [61], which looks to fulfill the condition $k_z = 2\pi/t$, where t is the disk thickness. This condition gives the energy for a cylinder standing wave whose nodes are at the disk faces. The disks measured here had $t \approx 100$ nm.

These two limits are illustrated in Fig. 6, where for modeling now we use the real part of the a -Si dielectric function (see Fig. 1). The two lowest-order modes can be seen in EELS maps for each of the five disks, and the mode energy as a function of disk diameter is plotted in the bottom row. Assuming a disk thickness of 100 nm and a beam energy of 300 keV, the waveguide model (lower dashed line) and “thin disk” approximation (upper dot-dashed line) in fact provide bounds on the observed mode energies for two lowest-energy waveguide modes, HE_{11} -type and TM_{01} -type modes. The experimental frequencies best match those predicted by the waveguide model for the disks whose diameter is smallest, which may be expected, as these are the only ones whose thickness is comparable to its diameter. However, we note that the additional dipole-type modes labeled with blue \times 's in the HE_{11} plot are not directly captured by the waveguide model but may represent modes which the waveguide model predicts will not be imaged, the TE_{01} modes, as discussed below.

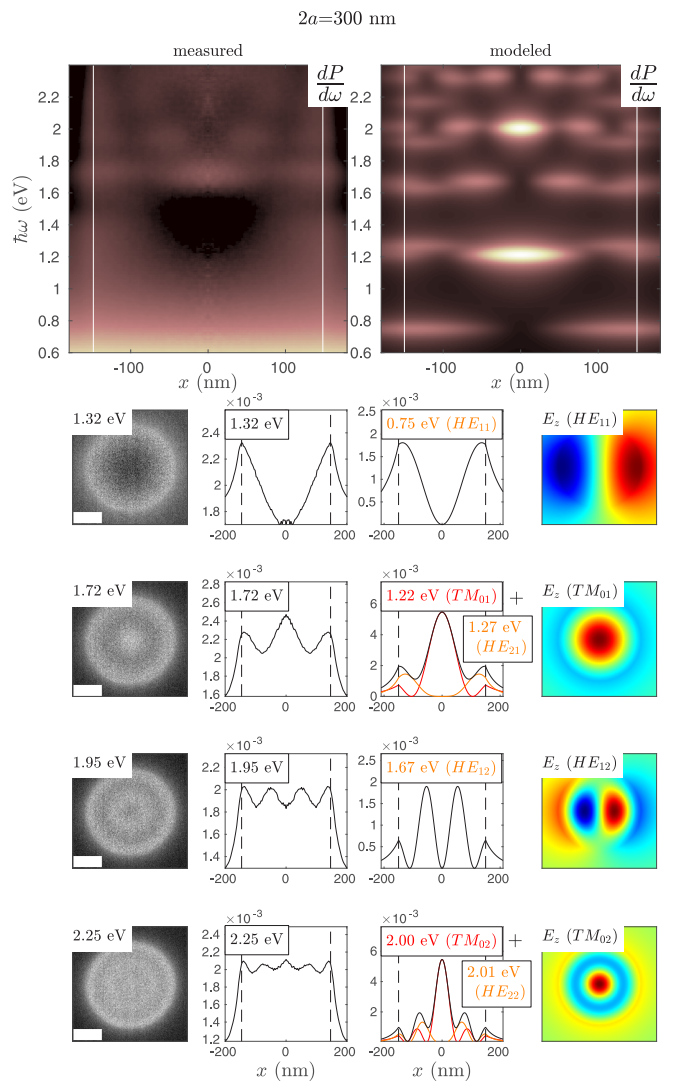


FIG. 7. Low-frequency modes for the $2a = 300$ nm disk. The top row shows idealized line scans from radially averaged data. Each of the four rows below this has a spectral map integrated over 0.1 eV from the unprocessed experimental data (far left), a reflected radial average of the experimental data (center left), a radial line scan of the predicted intensity from theoretical waveguide mode(s) (center right), and an in-plane map of E_z for the theoretical waveguide mode (far right). Dashed lines in the center columns represent cylinder edges, and scale bars on spectral maps represent 100 nm.

Looking in more detail at the 300 nm disk in Fig. 7 shows that the qualitative patterns observed in other low-order modes also match the patterns expected from the cylinder waveguide model. In the top row, where the radially averaged signal is shown on the left and the waveguide model prediction is shown on the right, the energy of the lowest order mode is not sharp, perhaps from the continued presence of two low-order modes. Even at higher energies, mode contributions are summed in the experimental spectrum. For instance, the summed contributions of the TM_{01} and HE_{21} modes in the waveguide model compare more favorably with the observed map variations at 1.72 eV than either model mode would on its own. This is also true when comparing the TM_{02} - and

HE₂₂-type modes in the waveguide model with the observed spatial variations in the STEM-EELS intensity at 2.25 eV.

V. DISCUSSION

The treatment above has focused on the middle ground between two better-studied extremes. One extreme involves narrow, thin samples and a moderately relativistic electron beam, where the electrostatic approximation in low-loss STEM-EELS often captures key features of EEL spectra. The other involves wide, thick geometries and a highly relativistic electron beam, in which case the Frank-Tamm formula for electrodynamic bulk loss is often appropriate. Yet here we have dealt with cases where the beam electron is swift enough to introduce fundamentally electrodynamic effects but where the sample geometry is not sufficiently extended to be described by bulk loss. When the dimensions of the sample and the wavelength of light in the material are comparable, and when the electron beam travels more quickly than the speed of light in a material, the possibility emerges for distinct, spatially-varying modes to appear in EEL spectral maps.

In Sec. II, outcomes of the electrostatic and electrodynamic models were compared for a thin ribbon of silicon in vacuum, which showed that electrostatic and electrodynamic models match at least qualitatively where the electron speed $v < c/\sqrt{\text{Re}[\epsilon]}$ when $\text{Re}[\epsilon] > 0$, and also when $\text{Re}[\epsilon(\omega)] < 0$. But where $v > c/\sqrt{\text{Re}[\epsilon]}$ and $\text{Re}[\epsilon] > 0$, waveguide modes emerge that are absent from the electrostatic description. In Sec. III, we developed these waveguide modes in an unbounded silicon cylinder, and in Sec. IV, we compared this model to the observed STEM-EEL signals from silicon disks. We note in passing that while the Fermi approach of Sec. II and the normal mode approach of Sec. III should be formally equivalent [62], the gap between one description and the other has not been fully bridged here. We have not dealt in the normal mode approach with the fact that the dielectric function is not strictly real-valued, which leads to nonradiative losses that merit a more involved quantized treatment [63].

More significantly, different descriptions of a system can lead to different conclusions about the causes of certain effects. For instance, sinusoidal variations of the waveguide modes along the cylindrical axis may exceed the thickness of the imaged sample, which Moreau *et al.* [47] concluded could lead to an EEL signal being spread over a wider range of frequencies. This is one possible explanation for why the lowest-order mode in the radially averaged signal of Fig. 7 seems to extend from 1.0–1.4 eV. Yet a more likely explanation is given in the optics literature [64,65]. Near the particular disk dimensions of those displayed in Fig. 7 ($d \approx 300$ nm,

$t \approx 100$ nm), the frequencies of the numerically calculated magnetic dipole (MD) and the electric dipole (ED) disk modes approach one another. These MD and ED modes are similar, respectively, to our HE₁₁ and TE₀₁ modes. And while the TE modes are *a priori* excluded from the waveguide description since $E_z = 0$ [see Eq. (13)], numerical calculations of similar modes [66] show how the electric field can stretch above and below the particle, providing one possible route toward imaging with EELS. Indeed, a higher order TE mode may be responsible for the “extra” dipole modes marked by the blue “×” labels in the lower left subplot of Fig. 6 above [41].

The above classifications are described more fully in a paper in preparation, in which STEM-EELS data from dielectric forms are interpreted by considering the electromagnetic resonances that may be excited in the nanostructures, with the eigenmodes determined using a numerical solver [41]. Complementary to the work presented here, this approach allows dielectric resonances to be compared across geometries. For instance, disk modes that we have identified as HE₁₁, TM₀₁, and HE₁₂ modes might relate, respectively, to MD, toroidal/vertical electric dipole, and a higher-order magnetic mode, an ordering in terms of ascending frequency that is reproduced in other geometries [65]. However, since this eigenmode approach does not determine the impulse response of STEM-EELS, it does not model the spectral data, in contrast to the approach using waveguide modes pursued here.

VI. CONCLUSION

At beam energies above the Cherenkov threshold, electrodynamic effects become increasingly important to low-loss STEM-EELS measurements as sample dimensions grow comparable to the wavelength of light in the material. Simulations for crystalline silicon nanoribbons indicate that the spatial variations of TE and TM waveguide modes may be observed in EELS data using a swift STEM beam ($v^2 > c^2/\epsilon$) when the ribbon width is ~ 100 nm. Simulations for silicon cylinders using waveguide modes are able to capture key low-order modes appearing in STEM-EELS measurements on disks of amorphous silicon whose diameters are in the range 100–500 nm. The lowest-energy modes in each disk resemble the HE₁₁ waveguide modes, and the next-to-lowest-energy modes resemble the TM₀₁ waveguide modes. For disks of thickness t , the unbounded cylinder model gives a lower bound on the experimental mode energy where $k_z = \omega/v$, and the “thin disk” model gives an upper bound on the experimental mode energy at $k_z = 2\pi/t$. Such limits help to establish guidelines for which STEM-EELS signals must be considered as essentially electrodynamic, where any electrostatic interpretation will be fundamentally unsuitable.

-
- [1] M. Haider, S. Uhlemann, E. Schwan, H. Rose, B. Kabius, and K. Urban, *Nature (London)* **392**, 768 (1998).
 [2] P. Batson, N. Dellby, and O. L. Krivanek, *Nature (London)* **418**, 617 (2002).
 [3] K. Kimoto, T. Asaka, T. Nagai, M. Saito, Y. Matsui, and K. Ishizuka, *Nature (London)* **450**, 702 (2007).

- [4] M. Bosman, V. J. Keast, J. L. García-Muñoz, A. J. D’Alfonso, S. D. Findlay, and L. J. Allen, *Phys. Rev. Lett.* **99**, 086102 (2007).
 [5] D. A. Muller, *Nat. Mater.* **8**, 263 (2009).
 [6] G. A. Botton, S. Lazar, and C. Dwyer, *Ultramicroscopy* **110**, 926 (2010).

- [7] H. Tan, S. Turner, E. Yücelen, J. Verbeeck, and G. Van Tendeloo, *Phys. Rev. Lett.* **107**, 107602 (2011).
- [8] H. L. Xin, C. Dwyer, and D. A. Muller, *Ultramicroscopy* **139**, 38 (2014).
- [9] K. Kimoto, *Microscopy* **63**, 337 (2014).
- [10] O. Krivanek, T. Lovejoy, M. Murfitt, G. Skone, P. Batson, and N. Dellby, *J. Phys.: Conf. Ser.* **522**, 012023 (2014).
- [11] O. L. Krivanek, T. C. Lovejoy, N. Dellby, T. Aoki, R. W. Carpenter, P. Rez, E. Soignard, J. Zhu, P. E. Batson, M. Lagos, R. F. Egerton, and P. A. Crozier, *Nature (London)* **514**, 209 (2014).
- [12] T. Miyata, M. Fukuyama, A. Hibara, E. Okunishi, M. Mukai, and T. Mizoguchi, *Microscopy* **63**, 377 (2014).
- [13] J. Nelayah, M. Kociak, O. Stéphan, F. J. García de Abajo, M. Tencé, L. Henrard, D. Taverna, I. Pastoriza-Santos, L. M. Liz-Marzán, and C. Colliex, *Nat. Phys.* **3**, 348 (2007).
- [14] M. Bosman, E. Ye, S. F. Tan, C. A. Nijhuis, J. K. W. Yang, R. Marty, A. Mlayah, A. Arbouet, C. Girard, and M. Y. Han, *Sci. Rep.* **3**, 1312 (2013).
- [15] E. P. Bellido, D. Rossouw, and G. A. Botton, *Microsc. Microanal.* **20**, 767 (2014).
- [16] M. Kociak and O. Stephan, *Chem. Soc. Rev.* **43**, 3865 (2014).
- [17] C. Cherqui, N. Thakkar, G. Li, J. P. Camden, and D. J. Masiello, *Annu. Rev. Phys. Chem.* **67**, 331 (2016).
- [18] P. A. Crozier, K. March, and Q. Liu, *Ultramicroscopy* **169**, 30 (2016).
- [19] C. Dwyer, T. Aoki, P. Rez, S. L. Y. Chang, T. C. Lovejoy, and O. L. Krivanek, *Phys. Rev. Lett.* **117**, 256101 (2016).
- [20] P. Rez, T. Aoki, K. March, D. Gur, O. L. Krivanek, N. Dellby, T. C. Lovejoy, S. G. Wolf, and H. Cohen, *Nat. Commun.* **7**, 10945 (2016).
- [21] G. Radtke, D. Taverna, M. Lazzeri, and E. Balan, *Phys. Rev. Lett.* **119**, 027402 (2017).
- [22] A. A. Govyadinov, A. Konečná, A. Chuvilin, S. Velez, I. Dolado, A. Y. Nikitin, S. Lopatin, F. Casanova, L. E. Hueso, J. Aizpurua, and R. Hillenbrand, *Nat. Commun.* **8**, 95 (2017).
- [23] M. J. Lagos, A. Trügler, U. Hohenester, and P. E. Batson, *Nature (London)* **543**, 529 (2017).
- [24] J. R. Jokisaari, J. A. Hachtel, X. Hu, A. Mukherjee, C. Wang, A. Konecna, T. C. Lovejoy, N. Dellby, J. Aizpurua, O. L. Krivanek, J.-C. Idrobo, and R. F. Klie, *Adv. Mater.* **30**, 1802702 (2018).
- [25] J. A. Hachtel, J. Huang, I. Popovs, S. Jansone-Popova, J. Keum, J. Jakowski, T. Lovejoy, N. Dellby, O. Krivanek, and J. C. Idrobo, *Science* **363**, 525 (2019).
- [26] K. Venkatraman, B. D. A. Levin, K. March, P. Rez, and P. A. Crozier, *Nat. Phys.* **15**, 1237 (2019).
- [27] F. S. Hage, G. Radtke, D. M. Kepaptsoglou, M. Lazzeri, and Q. M. Ramasse, *Science* **367**, 1124 (2020).
- [28] V. Myroshnychenko, J. Nelayah, G. Adamo, N. Geuquet, J. Rodriguez-Fernandez, I. Pastoriza-Santos, K. F. MacDonald, L. Henrard, L. M. Liz-Marzán, N. I. Zheludev, M. Kociak, and F. J. Garcia de Abajo, *Nano Lett.* **12**, 4172 (2012).
- [29] A. Polman, M. Kociak, and F. J. García de Abajo, *Nat. Mater.* **18**, 1158 (2019).
- [30] N. W. Bigelow, A. Vaschillo, V. Iberi, J. P. Camden, and D. J. Masiello, *ACS Nano* **6**, 7497 (2012).
- [31] M. Yurkin, V. Maltsev, and A. Hoekstra, *J. Quant. Spectrosc. Radiat. Transfer* **106**, 546 (2007).
- [32] F. J. García de Abajo and A. Howie, *Phys. Rev. B* **65**, 115418 (2002).
- [33] U. Hohenester, *Comput. Phys. Commun.* **185**, 1177 (2014).
- [34] F. J. García de Abajo, *Rev. Mod. Phys.* **82**, 209 (2010).
- [35] F. J. García de Abajo, N. Zabala, A. Rivacoba, A. G. Pattanyus-Abraham, M. O. Wolf, and P. M. Echenique, *Phys. Rev. Lett.* **91**, 143902 (2003).
- [36] N. Talebi, *J. Opt.* **19**, 23 (2017).
- [37] F. J. García de Abajo, *Phys. Rev. B* **59**, 3095 (1999).
- [38] A. Losquin and M. Kociak, *ACS Photonics* **2**, 1619 (2015).
- [39] T. Coenen, J. van de Groep, and A. Polman, *ACS Nano* **7**, 1689 (2013).
- [40] V. Flauraud and D. T. Alexander, *Microsc. Microanal.* **25**, 634 (2019).
- [41] V. Flauraud, F. Demming-Janssen, and D. T. L. Alexander (unpublished).
- [42] G. Boudarham and M. Kociak, *Phys. Rev. B* **85**, 245447 (2012).
- [43] D. Kordahl and C. Dwyer, *Phys. Rev. B* **99**, 104110 (2019).
- [44] D. E. Aspnes and A. A. Studna, *Phys. Rev. B* **27**, 985 (1983).
- [45] G. Jellison, *Opt. Mater. (Amsterdam)* **1**, 41 (1992).
- [46] S. Adachi, *Phys. Rev. B* **38**, 12966 (1988).
- [47] P. Moreau, N. Brun, C. A. Walsh, C. Colliex, and A. Howie, *Phys. Rev. B* **56**, 6774 (1997).
- [48] M. Couillard, A. Yurtsever, and D. A. Muller, *Phys. Rev. B* **77**, 085318 (2008).
- [49] P. M. Echenique and J. B. Pendry, *J. Phys. C* **8**, 2936 (1975).
- [50] R. Garcia-Molina, A. Gras-Marti, A. Howie, and R. H. Ritchie, *J. Phys. C* **18**, 5335 (1985).
- [51] J. P. R. Bolton and M. Chen, *J. Phys.: Condens. Matter* **7**, 3389 (1995).
- [52] A. Howie, *Ultramicroscopy* **203**, 52 (2019).
- [53] D. Kordahl, Ph.D. thesis, Arizona State University, 2020.
- [54] R. Sammut and A. W. Snyder, *Appl. Opt.* **15**, 477 (1976).
- [55] S. Yang and J.-M. Song, *Prog. Electromagn. Res. B* **66**, 143 (2016).
- [56] J. A. Stratton, *Electromagnetic Theory*, 1st ed. (McGraw-Hill, New York, 1941).
- [57] E. Snitzer, *J. Opt. Soc. Am.* **51**, 491 (1961).
- [58] C. Yeh and F. I. Shimabukuro, *The Essence of Dielectric Waveguides* (Springer US, Boston, 2008).
- [59] A. Khrennikov, B. Nilsson, S. Nordebo, and I. Volovich, *AIP Conf. Proc.* **1508**, 285 (2012).
- [60] A. A. Lucas, E. Kartheuser, and R. G. Badro, *Phys. Rev. B* **2**, 2488 (1970).
- [61] G. Zaretskaya, A. V. Drozdovskii, A. B. Ustinov, and B. A. Kalinikos, *J. Phys.: Conf. Ser.* **1038**, 012099 (2018).
- [62] Z. Wang, *Micron* **27**, 265 (1996).
- [63] D. Marcuse, *Principles of Quantum Electronics* (Academic Press, New York, 1980).
- [64] J. van de Groep and A. Polman, *Opt. Express* **21**, 26285 (2013).
- [65] I. Staude, A. E. Miroshnichenko, M. Decker, N. T. Fofang, S. Liu, E. Gonzales, J. Dominguez, T. S. Luk, D. N. Neshev, I. Brener, and Y. Kivshar, *ACS Nano* **7**, 7824 (2013).
- [66] M. Decker and I. Staude, *J. Opt.* **18**, 103001 (2016).